Chemical Science

ROYAL SOCIETY OF CHEMISTRY

EDGE ARTICLE

View Article Online
View Journal | View Issue

Cite this: *Chem. Sci.*, 2026, **17**, 307

All publication charges for this article have been paid for by the Royal Society of Chemistry

Received 15th August 2025
Accepted 6th November 2025

DOI: 10.1039/d5sc06225j

rsc.li/chemical-science

Reaction-pathway resolved multimode imaging of electrocatalytic oxygen evolution on single silver nanowires@ITO Mott–Schottky junctions

Yu Cui, Lisi Wen, Houkai Chen, Guopeng Li, Zhe Zhang and Rui Hao *

Mott–Schottky junctions are considered an ongoing focus in electrocatalysis due to their unique ability to modulate charge distribution, thereby improving the performance of electrocatalysts. However, resolving the interfacial reaction mechanism with high spatiotemporal and chemical resolution *in situ* remains challenging. Herein, a time-synchronized multimode optical imaging platform is developed, realizing multi-perspective visualization of a model Mott–Schottky (MS) electrocatalytic system. The unique interfacial electrooxidation dynamics of the individual silver nanowires (AgNWs) on an ITO substrate (AgNWs@ITO) MS junction and associated electrocatalytic oxygen evolution reaction (OER) pathways are revealed. The MS effect has been proven to regulate the reaction mechanisms by redistributing interfacial charges, leading to the superoxide radical-mediated reaction pathway. Thus, the superoxide radical scavengers can exclusively exert regulatory effects on AgNWs@ITO. Moreover, the finding highlights the possible active role of ITO in electrocatalytic studies. The unveiled modulating effect of the Mott–Schottky nanostructure on the electrochemical reaction pathway shows the potential and importance of the multi-resolved imaging approach in analyzing fundamental mechanisms of heterogeneous catalysis.

Introduction

Mott–Schottky junctions could form through the contact between a metal and a semiconductor,[1] such as by dispersing the metal on the surface of the semiconductor electrode or *vice versa*, and are emerging as favored architectures in electrocatalysis.[2] The heterojunctions facilitate significant progress in energy-related conversion processes, including hydrogenation,[3] aerobic oxidation,[4] artificial photosynthesis,[5] water splitting,[6] and more. Their effectiveness arises from the ability to speed up interfacial charge transfer, modulate charge distribution, and control the chemisorption energies of reactive species—key characteristics vital for tuning catalytic activity.[1,7,8]

Water electrolysis is one of the important ways for the sustainable production of clean energy. The oxygen evolution reaction (OER), as a critical half-reaction, requires the concerted transfer of four protons and electrons, with its sluggish kinetics posing a major bottleneck for overall energy conversion efficiency.[9,10] Mott–Schottky junctions could play important roles in designing high-performance OER electrocatalysis. For instance, Ru–RuO_2 Schottky nanojunctions are found to be highly effective for inhibiting the overoxidation of RuO_2 for extended durability in acidic water-oxidation.[11] Silver-based OER catalysts have been extensively studied due to their cost-effectiveness and superior conductivity.[12] Ag nanoparticles (AgNPs) were anchored on CoV-LDH@graphene nanosheets to form a Mott–Schottky heterojunction, promoting the deprotonation of *OOH and enhancing electron transfer kinetics.[13] Despite the progress, a deep understanding of the relationship between Mott–Schottky heterostructures and the OER activities is essential for developing novel and highly efficient electrocatalysts.

Currently, the exploration of Mott–Schottky junctions is mainly conducted through evaluating the electronic states of catalysts and measuring their work functions *via* ultraviolet photoelectron spectroscopy (UPS) in a vacuum environment.[14–16] However, this method is an overall testing approach that lacks spatial resolution. Although measurements at the microscopic level can be accomplished through Kelvin probe force microscopy (KPFM),[17–19] which is used for detecting the surface potential difference and work function of heterogeneous catalysts,[20] it is still challenging to obtain dynamic charge information in practical catalytic environments. The Mott–Schottky effect can also be understood and predicted through DFT calculations,[21–23] but there are often discrepancies between theoretical analysis and the actual catalytic behavior.

Recent advances in optical imaging technologies have opened avenues for probing electrochemical interfaces with high spatiotemporal and chemical resolutions.[24–27] Single-mode imaging techniques (*e.g.*, plasmonic microscopy,[28] fluorescence mapping,[29,30] or dark field microscopy[31,32]) provide

Department of Chemistry, Research Center for Chemical Biology and Omics Analysis, Shenzhen Key Laboratory of Functional Proteomics, Southern University of Science and Technology, 518055, Shenzhen, China. E-mail: haor@sustech.edu.cn

valuable insights into specific aspects of interfacial reactions, such as localized pH gradients,[33,34] molecular adsorption–desorption kinetics,[35,36] or vibrational mode changes.[37,38] By coupling optical observation and the electrochemical process, these techniques enable researchers to conduct an intuitive, visualized, and dynamic analysis of the interfacial electrocatalysis at the single-nano-entity scale.[39,40] However, single-mode imaging approaches inherently lack the multidimensionality required to reconstruct reaction pathways with full details. This limitation highlights the necessity for correlated multimodal imaging strategies, which synchronize complementary techniques to capture interdependent electronic, chemical, and morphological transformations in real time.[41–43]

In this work, we developed a time-synchronized multimodal optical imaging platform integrating epi-illumination microscopy (Epi) and electrochemiluminescence (ECL) imaging. This system enables simultaneous visualization of interfacial charge transfer dynamics and reactive oxygen species generation with nanoscale spatial resolution. ITO, a widely used substrate in electrocatalytic optical imaging, is adopted due to its high transparency, electrical conductivity, and relatively low electrocatalytic activity.[44] Unlike conventional studies that overlook ITO's influence, we consider its impact on the catalytic interface and use it as the semiconductor side of the Mott–Schottky junction. By loading metal materials on its surface, we conveniently constructed a Mott–Schottky model system conducive to the optical observation platform.

Taking advantage of this model system, we investigated the electrochemical oxidation of AgNWs and its associated OER—an ideal framework to probe interfacial charge redistribution at Mott–Schottky junctions formed between AgNWs and the ITO substrate. By synergizing spatially resolved optical signals with *in situ* electrochemical measurements, we achieved the resolution of a unique reaction pathway mediated by superoxide radicals driven by Mott–Schottky at the single-nanostructure level. Further analysis reveals that the charge rearrangement caused by the Mott–Schottky junctions enriches electrons on the AgNWs, which affects the adsorption of substances in the surroundings, thus influencing the reaction kinetics and altering the reaction pathway. This work not only advances the fundamental understanding of Mott–Schottky electrocatalysis but also establishes a versatile framework for resolving pathways of heterojunction-based catalytic systems through direct mechanistic visualization.

Results and discussion

Reaction pathway resolved multimodal imaging of AgNWs@ITO

Here we constructed a time-synchronized multimode imaging microscope for electrochemical interface monitoring, as shown in Fig. 1a. The electrochemiluminescence emission wavelength of luminol (LMN) is around 425 nm.[45] Epi imaging is performed using a light source with a wavelength range of 625 ± 26 nm. The wavelength difference between the two is enough to allow us to achieve the independence of the two light paths through the rational design of the optical path and the appropriate matching of filters. The reflection signal of *in situ* Epi imaging can be detected using an sCMOS camera, while the *in situ* ECL signal can be recorded using an electron-multiplying CCD (EMCCD) with high EM-gain (EM gain = 800). Detailed information is provided in the Experimental section. Commercially available AgNWs with a diameter of 120 nm were drop-cast onto the substrates (Fig. S1) to form an AgNWs@ITO structure.

When a linear sweep voltammetry (LSV) scan was applied to the interface in 0.1 M NaOH containing 1 mM LMN, with the potential ranging from 0 V to + 2 V with respect to the home-made Ag/Ag_2O electrode,[43,46,47] the AgNWs underwent electrochemical oxidation. The standard reduction potential of the Ag/Ag_2O reference electrode ($Ag_2O/AgOH^-$) is 0.343 V *vs.* the standard hydrogen electrode (SHE),[47] while in our system at pH 13, the electrode potential is 1.169 *vs.* the reversible hydrogen electrode (RHE). Fig. 1b presents the snapshots of individual AgNWs at different potentials during the evolution process in both modes. The concentration of the AgNW dispersion was adjusted to 30 μg mL^{-1} to achieve single nanowire observation. Due to their high reflectivity, single AgNWs (1#, 2#, and 3#) manifested a pronounced positive contrast in the images. As the potential was scanned towards the positive direction, no observable changes were detected on the AgNWs before 1 V, as referred to in the horizontal part of the intensity curve in Fig. 1c. With the potential increased to 1.07 V, it was evident that 1# darkened rapidly, signifying that the surface of the original metallic Ag had been electrochemically oxidized. It is generally acknowledged that the reflectivity of metal oxides is lower than that of metals. Consequently, the reflective intensity diminished, and the AgNWs exhibited a negative contrast pattern, corresponding to the sharp decline on the intensity curve as depicted in Fig. 1c. As the potential continued to increase, 2# and 3# were oxidized at 1.12 V and 1.35 V, respectively. This difference in oxidation potential is most likely an integrated effect combining the heterogeneity between the AgNWs and the difference in their electrical contact with the substrate.[48,49] The Epi intensity curve exhibited a drastic increase after 1.5 V. This was caused by the generation of bubbles catalyzed by silver oxides at the interface, which show high positive contrast in the Epi imaging mode.

In the ECL mode, EMCCD obtained a clear ECL signal (Fig. 1b, bottom section) while the AgNWs were oxidized. The ECL intensity increased while the Epi reflection intensity decreased, as shown in Fig. 1c. This phenomenon implies that concurrent with the oxidation of the AgNWs, a specific substance triggers the luminescence response of LMN molecules. In light of LMN's luminescence mechanism, we presume that reactive oxygen species (ROS) play a part in this process.[45,50] The spreading of the luminescence signal in the ECL images should be due to the diffusion of free radicals.

The relationship between the ECL intensity and the LMN concentration was explored, and the resultant data are presented in Fig. 1d. The luminescence intensity positively correlated with the concentration ranging from 1 mM to 5 mM. The snapshots of peak intensity at concentrations of 2 mM and 5 mM are shown in Fig. 1e. Meanwhile, we noticed that as the LMN concentration rose, the luminescence starting potential

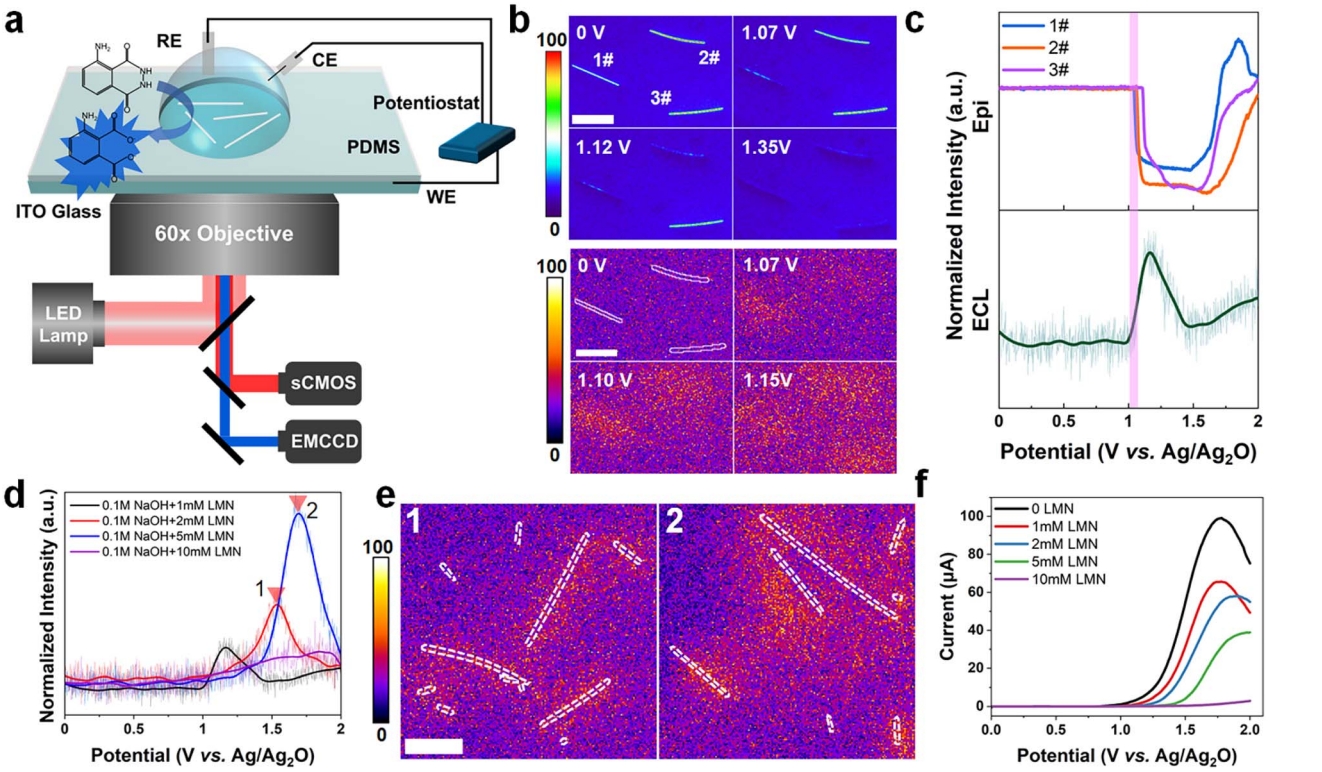

Fig. 1 (a) Schematic diagram of time-synchronized multimodal imaging. (b) Images in the Epi mode (upper part) and the ECL mode (lower part) at different potentials in 0.1 M NaOH containing 1 mM LMN. (c) Curves of the change in Epi intensity (upper part) and ECL intensity (lower part) with voltage. (d) The ECL intensity curves changing with voltage at different concentrations of LMN molecules. (e) ECL images corresponding to positions 1 and 2 in (d). (f) LSV curves at different LMN concentrations. All scale bars: 10 μm.

was progressively delayed. Specifically, at 1 mM, 2 mM, and 5 mM, the luminescence starting potentials were measured to be 0.99 V, 1.13 V, and 1.24 V, respectively. On further increasing the concentration to 10 mM, no ECL signal could be detected, indicating that the electrooxidation of AgNWs was blocked (Fig. S2). These findings point out that the electrochemical oxidation of AgNWs could be postponed or even completely inhibited with an increased LMN concentration. The corresponding LSV curve is illustrated in Fig. 1f. Evidently, not only did the peak current diminish gradually, but also the onset potential shifted in the positive direction as the LMN concentration augmented. We can unambiguously deduce that LMN molecules exert an inhibitory influence on the electrochemical oxidation of AgNWs, and this effect becomes more pronounced with the increasing LMN concentration until the oxidation process is fully suppressed. The substance responsible for inducing ECL also constitutes a crucial part of the electrochemical oxidation process of AgNWs@ITO.

Modulatory effect of *p*-BQ on reaction pathways

We speculate that the reason for luminol inhibiting the electrochemical oxidation of AgNWs@ITO is that it can consume free radicals. To further explore the oxidation mechanism of AgNWs and unravel the pivotal role of free radicals in this process, we introduced *p*-BQ, a typical superoxide radical scavenger,[51,52] into our system. We correlated the *p*-BQ concentration with solution pH and found negligible pH variations when the *p*-BQ concentration was less than 20% of the main solute (Fig. S3). Since we control the concentration of *p*-BQ at 10% of the main solute, it is reasonable to assume that the experimental results caused by *p*-BQ are not related to the pH changes it induced, but rather only related to its presence.

LSV curves tested in electrolytes with and without *p*-BQ are shown in Fig. 2a. The OER current was suppressed to 2.75 μA at even 2 V while *p*-BQ exists, at the same level as the bare ITO with no modification (Fig. S4). When the solution was replaced, the current at 2 V surged significantly to 29.55 μA. The Epi images corresponding to the LSV process at different voltages are shown in Fig. 2c. In the presence of *p*-BQ (top row), the AgNWs remained intact at the ITO interface. Conversely, once *p*-BQ was removed (bottom row), the same AgNWs gradually underwent electrooxidation. Correspondingly, their reflection intensity curves in the Epi mode also exhibit a striking contrast, with one demonstrating negligible change and the other a precipitous fall (Fig. 2b). Considering the possibility that this phenomenon arises from the electron tunneling effect of the modification layer, we investigated the electrochemical behavior of AgNWs on an unmodified substrate, as shown in Fig. S5. The results are basically consistent with those of the modified substrates, indicating that this phenomenon is irrelevant to the modified layer. The LSV curves and the Epi images before and after the reaction in the dark environment are presented in Fig. S6. This

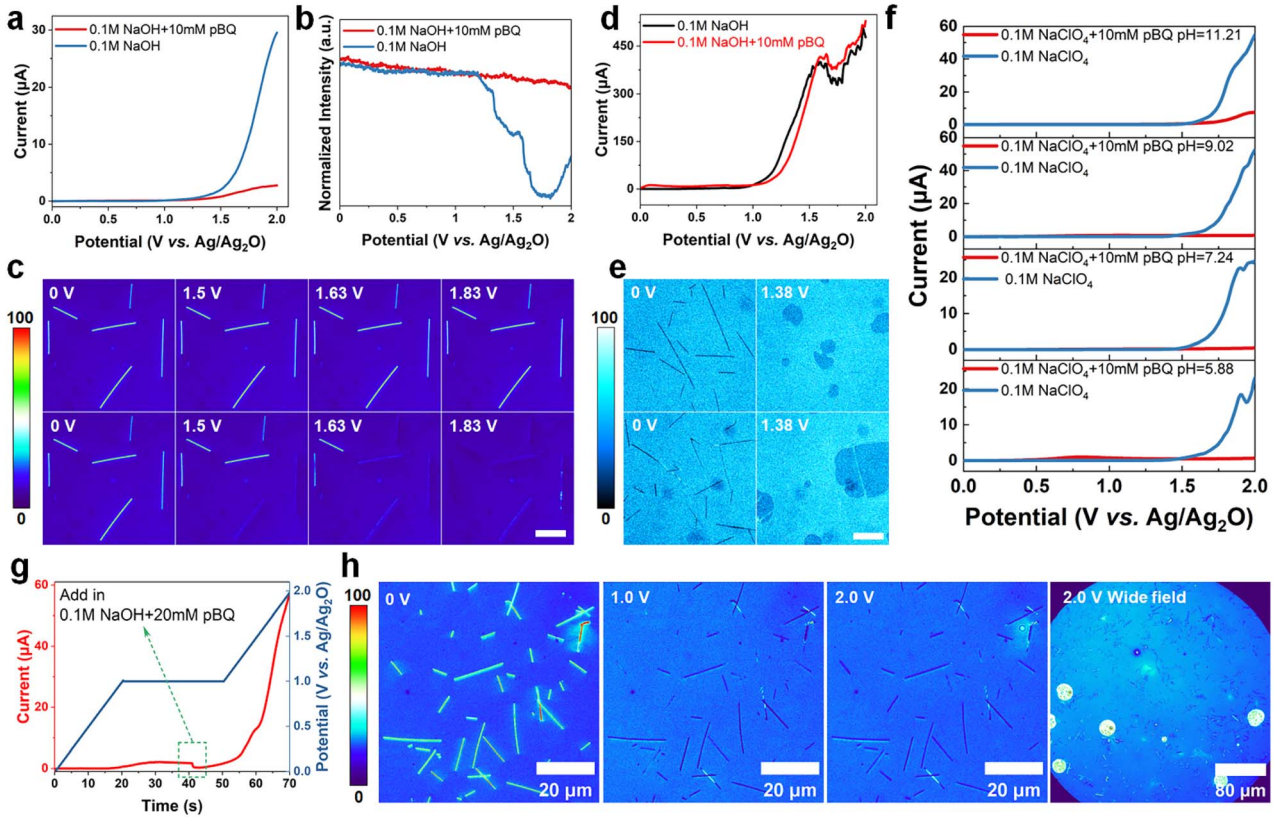

Fig. 2 (a) LSV curves in electrolytes with and without *p*-BQ on the ITO interface. (b) Epi intensity curves plotted *vs.* potential in electrolyte with and without *p*-BQ. (c) Snapshots at different voltages corresponding to the LSV process in (a): with (upper row) and without (lower row) *p*-BQ. Scale bar: 10 μm. (d) LSV curves in electrolytes with and without *p*-BQ on the Au interface. (e) Snapshots at different voltages corresponding to the LSV process in (d): with (upper row) and without (lower row) *p*-BQ. Scale bar: 10 μm. (f) LSV curves in solutions with different pH values. (g) Potential and current curves changing with time in the electrochemical test. The initial electrolyte is 10 μL 0.1 M NaOH. During 0–20 s, voltage increases linearly from 0 V to 1 V. During 20–50 s, a constant voltage of 1 V is maintained for 30 s to ensure the complete oxidation of AgNWs. During 50–70 s, voltage increases linearly from 1 V to 2 V. 10 μL 0.1 M NaOH + 20 mM *p*-BQ is added at 41 s. (h) Epi images at different voltages and a wide field of view at 2 V.

demonstrates that the electrooxidation and OER on AgNWs and the modulation effect of *p*-BQ are unrelated to the red light used in Epi mode and the potential thermal effects it induces. To further ascertain the dominant role of superoxide radicals, a typical radical sacrificial agent for hydroxyl radicals, tertiary butanol (*t*-BA),[51,53] was also investigated. The results showed that *t*-BA cannot regulate the electrochemical process of AgNWs@ITO when its concentration is fixed at 10 mM and this inability persisted even when the concentration was increased tenfold (Fig. S7). In this case, we believe that hydroxyl radicals have a negligible effect on the electrooxidation of AgNWs@ITO. These outcomes perfectly meet our anticipation that the superoxide radicals induce direct oxidation of AgNWs@ITO.

We assume that the AgNWs@ITO structure induces the superoxide radical involved reaction pathway. Hence, the electrooxidation behavior of AgNWs on metallic substrates was further explored, wherein the prevalently utilized Au substrate was adopted (denoted as AgNWs@Au). As presented in the LSV data in Fig. 2d, the electrochemical behavior of AgNWs remained essentially consistent both in the presence and absence of *p*-BQ. Merely, the onset potential exhibited a marginal delay in the electrolyte containing *p*-BQ. Fig. 2e presents the images at varying voltages in electrolyte with (top row) and without (bottom row) *p*-BQ. Unlike the ITO surface, the Au surface has a higher reflectivity, resulting in a negative contrast pattern of AgNWs. When the voltage was scanned to 1.38 V, AgNWs were oxidized and significant OER arose in both electrolytes. The results showed no obvious difference when the Au layer was modified using poly-tyramine (Fig. S8).[54] The negligible inhibitory effect of *p*-BQ on AgNWs@Au suggests that its effectiveness on AgNWs@ITO is unlikely to be attributed to the adsorption of *p*-BQ. Furthermore, it demonstrates that superoxide radicals may not serve as the primary reactive species in the electrochemical oxidation of AgNWs@Au, indicating that the electrochemical oxidation of AgNWs@ITO follows a completely distinct electrochemical reaction pathway. Furthermore, we conducted experiments in electrolytes with pH values ranging from 5.88 to 11.21. The pH value was adjusted with NaOH. The LSV curves are shown in Fig. 2f, showing that the OER current was suppressed when *p*-BQ existed. The corresponding Epi images are shown in Fig. S9. Once *p*-BQ was removed, bubbles appeared at the interface. These results

indicate that this particular reaction pathway is not pH-dependent; it is attributed to the unique interface structure formed between AgNWs and the ITO surface.

Whether the inhibition of the OER by *p*-BQ occurs during the electrochemical oxidation stage of AgNWs or the OER stage is quite important for analyzing the reaction mechanism. Therefore, we pre-oxidized the AgNWs and then added *p*-BQ during the continuous electrochemical test. For details, see the electrochemical test section in the SI. *p*-BQ was added at 41 s, as manifested in Fig. 2g. The corresponding snapshots are shown in Fig. 2h. It can be seen that all the AgNWs have been oxidized during the constant voltage stage. When the voltage reached 2 V, bubbles appeared even when *p*-BQ was already added. In the larger field of view area, the oxygen evolution at the interface is quite obvious, which indicates that *p*-BQ has no obvious inhibitory effect on the OER of the already oxidized AgNWs.

As analyzed, the superoxide radical-related reaction pathway highly relies on AgNWs-ITO contact, which can be easily regulated by adjusting the concentration of the AgNW drop-casting solution. The relationship between the suppression effect of *p*-BQ and the AgNW dispersion concentration was studied. LSV curves are shown in Fig. 3a. As the AgNW concentration decreases, OER current diminishes and onset potential shifts positively. When the concentration was reduced to 30 μg mL^{-1}, the electrooxidation of AgNWs and the OER were occluded. Note that at 500 μg mL^{-1}, an oxidation peak appears from 0.81 V to 1.1 V, which occurs nearly simultaneously with the decrease in reflection intensity in Epi mode, as shown in Fig. 3b, indicating that the intensity drop is caused by the oxidation of AgNWs. Fig. 3c shows Epi images at different voltages during LSV. Evidently, the AgNW concentration significantly affects its distribution at the ITO interface. At high concentrations, the AgNWs are densely stacked, and most of the AgNWs-solution contact regions were distant from the ITO interface. The AgNWs-ITO contact can no longer alter the electrochemical properties of these regions. Consequently, these regions still follow the reaction pathway where superoxide radicals play little to no role, leading to the inefficiency of *p*-BQ. When the concentration was 100 μg mL^{-1} and 50 μg mL^{-1}, the oxidation and OER behavior were observed on part of the AgNWs, while another part remained unchanged. When the concentration was reduced to 30 μg mL^{-1}, the AgNWs remained bright in the Epi images even when the voltage was increased to 2 V, meaning that AgNWs@ITO junctions formed on the entire ITO surface. Therefore, in the previous experiment, it is reasonable for us to fix the AgNW concentration at 30 μg mL^{-1}.

Next, we fixed the concentration of AgNWs at 30 μg mL^{-1} and adjusted the concentration of *p*-BQ in 0.1 M NaOH solution to explore the inhibiting effect. The results are exhibited in Fig. 3d. As shown, when the *p*-BQ concentration increased from 0 mM to 10 mM, the onset potential gradually shifted positively, and the peak current gradually decreased. This indicates that the inhibitory effect of *p*-BQ becomes stronger with the increase in the concentration. On further increasing the *p*-BQ concentration to 8 mM, the OER current is reduced to 2.7 μA, nearly the same as the case when the concentration was increased to 10 mM. This indicates that the inhibitory effect of *p*-BQ has already reached saturation, and reactions are suppressed. After

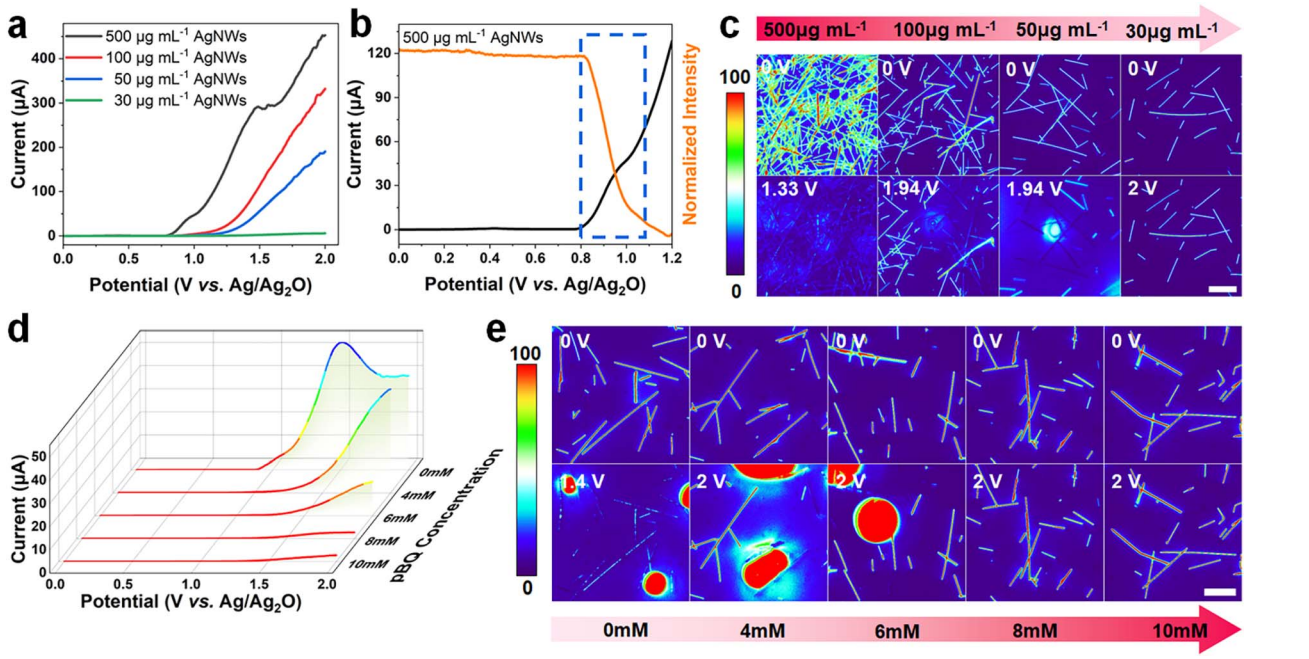

Fig. 3 (a) LSV curves with different amounts of AgNWs loaded on the modified ITO substrate in 0.1 M NaOH + 10 mM *p*-BQ. (b) 0–1.2 V LSV curve and the Epi intensity–voltage curve when the concentration of AgNW drop casting solution is 500 μg mL^{-1}. (c) Snapshots at different voltages corresponding to the LSV process in (a) with concentrations of AgNW drop casting solution ranging from 500 μg mL^{-1} to 30 μg mL^{-1}. (d) LSV curves in electrolytes with varied *p*-BQ concentrations in 0.1 M NaOH on the modified ITO interface. (e) Snapshots at different voltages corresponding to the LSV process in (d). All scale bars: 10 μm.

replacing the electrolytes with solutions not containing *p*-BQ in these almost fully suppressed cases, we can see from the LSV curves that the OER recurred (Fig. S10a), and only the peak current decreased which might be attributed to the incomplete removal of *p*-BQ. Epi images at different voltages at different *p*-BQ concentrations are shown in Fig. 3e. As shown, the electrochemical behavior of AgNWs exhibits a trend of complete oxidation–partial oxidation–negligible oxidation. After the replacement of the solution, the superoxide radical pathway reoccurred (Fig. S10b). The inhibitory effect of *p*-BQ and similar trends still persisted even when we used 1 M NaOH electrolyte solution which is more conducive for oxidation and the OER to take place (Fig. S11). These results further corroborate our prior inference that the contact between AgNWs and ITO modifies the reaction pathway. Additionally, they imply that the inhibitory effect of *p*-BQ necessitates a well-formed AgNWs@ITO Mott–Schottky junction and a specific *p*-BQ concentration threshold.

The influence of the AgNWs@ITO Mott–Schottky junctions on reactions

The formation of the AgNWs@ITO heterojunctions will affect the electrooxidation pathway of AgNWs and thereby the OER process. Therefore, we studied the changes in the oxidation peak when the AgNWs@ITO heterojunction gradually formed. We analyzed the LSV process of the AgNWs at a slow scan rate in 0.1 M NaOH. Normally, three typical oxidation peaks will appear when the Ag plate electrode is electrooxidized,[55] as shown in Fig. 4a:

$$\text{A1: Ag (s)} + 2\text{OH}^- \text{ (aq)} \rightleftarrows \text{Ag(OH)}_2^- \text{ (aq)} + \text{e}^-$$

$$\text{A2: 2Ag (s)} + 2\text{OH}^- \text{ (aq)} \rightleftarrows \text{Ag}_2\text{O (s)} + \text{H}_2\text{O (l)} + 2\text{e}^-$$

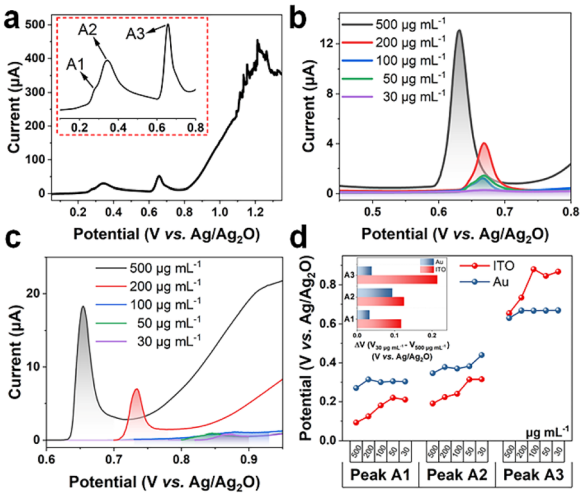

Fig. 4 (a) The LSV curve of the silver disk electrode (diameter: 2 mm) in 0.1 M NaOH. The red dashed box is the enlarged view of A1, A2 and A3 oxidation peaks. (b) The A3 oxidation peak of AgNWs on the Au substrate. (c) The A3 oxidation peak of AgNWs on the ITO substrate. (d) The potential statistical chart of the A1, A2 and A3 oxidation peaks on the Au and ITO substrates. The inserted graph shows the potential differences in the A1, A2 and A3 oxidation peaks when the concentration of AgNWs is 30 μg mL^{-1} and 500 μg mL^{-1}.

$$\text{A3: Ag}_2\text{O (s)} + 2\text{OH}^- \text{ (aq)} \rightarrow 2\text{AgO (s)} + \text{H}_2\text{O (l)} + 2\text{e}^-$$

The oxidation peaks of AgNWs with different concentrations on Au and ITO substrates are shown in Fig. S12a and c. The higher the concentration of AgNWs, the more obvious the oxidation peak and the greater the oxidation current. The A1 and A2 peaks on Au and ITO are shown in Fig. S12b and d, and the A3 peaks are shown in Fig. 4b and c. The potentials of A1, A2, and A3 are summarized in Fig. 4d. As the concentration of AgNWs decreases, the potentials of A1 and A2 on both the Au and ITO interfaces gradually shift positively, showing almost the same trend. Nevertheless, the potential of A3 on the ITO interface increases significantly as the concentration of AgNWs decreases, but the change on the Au interface is minimal. We further statistically analyzed the potential differences in the three oxidation peaks when the interface was dominated by the Schottky structure (concentration at 30 μg mL^{-1}) and by AgNWs (concentration at 500 μg mL^{-1}), and the results are presented in the inset of Fig. 4d. We can observe more clearly that the magnitudes of the positive shifts of the three oxidation peaks on ITO are all greater than those on Au, and the variation magnitude of A3 is the largest. This indicates that the Mott–Schottky heterojunction mainly affects the A3 oxidation process of AgNWs on the ITO interface, which is consistent with the abovementioned phenomenon that the ECL signal only appears during the high-valence oxidation of AgNWs. Moreover, at low concentrations, the AgNWs@ITO structure tends to be perfect, and the potential of A3 on the ITO interface accordingly tends to be stable.

This particular reaction pathway of AgNWs at the ITO interface is attributed to the Mott–Schottky junctions formed between the two, as illustrated in Fig. 5a. When a metal comes into contact with a semiconductor, electrons spontaneously migrate from the side with a lower work function to the other, forming the Mott–Schottky junction.[1,17] This process leads to the equilibrium of the Fermi level, inducing the bending of the semiconductor energy band and generating a built-in electric field. The Mott–Schottky effect redistributes electrons, which leads to the transformation of the electronic states on both sides of the interface and adjusts the adsorption status of small molecules at the interface in the liquid phase environment. In our case, the work functions (Φ) of ITO and Ag were calculated to be 3.805 eV and 4.615 eV respectively using the formula:[15]

$$\Phi = h\gamma - E_{\text{cutoff}}$$

where $h\gamma$ is 21.22 eV and E_{cutoff} was determined by extrapolating the linear section of the UPS to the baseline (Fig. S13).[15] Note that the samples for Ag were prepared by coating a 100 nm Ag layer on ITO, for the measurement of the work function of bulk silver. Considering the sparse distribution of AgNWs and the insufficient spatial resolution of UPS measurements, it is relatively difficult to directly obtain the work function of AgNWs. Here, we use the work function of the Ag layer as a substitute for the work function of AgNWs to estimate the electron flow direction. According to the formula:[15]

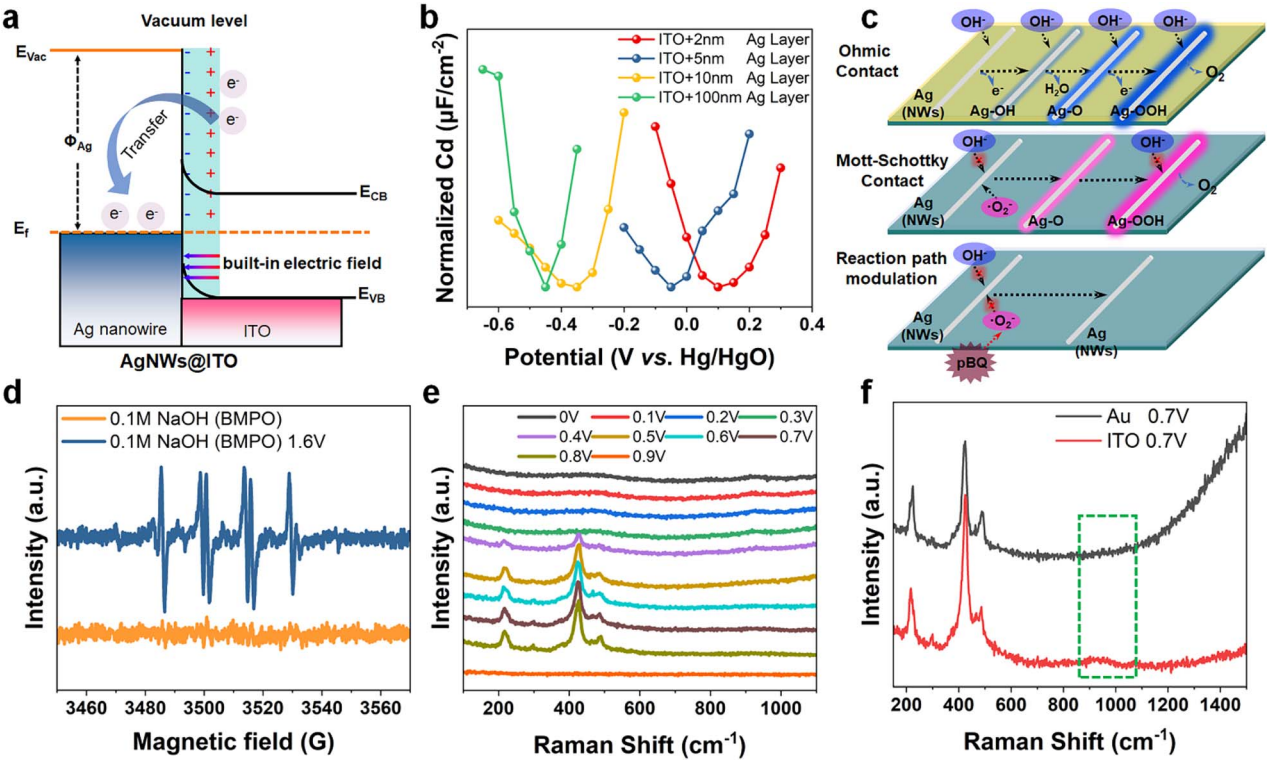

Fig. 5 (a) Energy band diagram of the AgNWs@ITO Mott–Schottky junction. (b) Normalized differential capacitance curves of a silver layer coated on ITO with different thicknesses. (c) Schematic of the reaction pathways of AgNWs on Au, the ITO surface and the *p*-BQ modulation. (d) Electron paramagnetic resonance spectra of AgNWs at the ITO interface after conducting a chronoamperometry test. (e) *In situ* Raman spectrum of AgNWs on modified ITO in 0.1 M NaOH. (f) *In situ* Raman spectra of AgNWs on Au and ITO substrates at 0.7 V.

$$W = W_{\text{bulk}} + \frac{1.08}{d}$$

where W is the work function and d is the diameter of the metal nanoparticle, the work function of nanoparticles is higher than that of their bulk counterparts, so this substitution is reasonable. Given this difference in the work function, Mott–Schottky junctions are formed between AgNWs and ITO, and electrons transfer from ITO to Ag with a Mott–Schottky barrier of 0.81 V. To further demonstrate this electron enrichment, we tested the potential of zero charge (PZC) of silver layers with varying thicknesses deposited on ITO substrates within 1 mM NaOH solution.[56] The differential capacitance curve is presented in Fig. 5b. As the thickness of the silver layer diminishes from 100 nm to 2 nm, PZC gradually increases from −0.45 V to 0.1 V (*vs.* Hg/HgO).[57–59] This positive shift clearly indicates that the thinner the silver layer, the higher the concentration of negative charge.[60,61] A visual illustration of this relationship is presented in Fig. S14. As AgNWs come into contact with ITO, they will be negatively charged as electrons spontaneously transfer from ITO to AgNWs.

The OER process in alkaline solution is very intricate, and the generally accepted mechanism is the Adsorption Evolution Mechanism (AEM).[62] Normally, the OER commences with the adsorption of OH^- onto the active site of the electrocatalyst.[63] As depicted in Fig. 5c, an ohmic contact is formed between AgNWs and the metal interface, and OH^- is adsorbed onto the active sites on the surface of AgNWs, resulting in the formation of Ag–OH. Further adsorption leads to the transformation of Ag–OH into Ag–O. Through additional adsorption steps, Ag–O converted into Ag–OOH. Then another OH^- is adsorbed to Ag–OOH and finally leads to the release of oxygen. Superoxide radicals do not appear to be involved in this process; thus *p*-BQ cannot suppress this process as we confirmed before.

When AgNWs are on the ITO interface, the negative charge accumulates on the surface of AgNWs due to the formation of Mott–Schottky junctions, which makes it difficult for OH^- to adsorb. More importantly, the electrons are likely captured by dissolved oxygen to form superoxide radicals.[64–66] Electron Paramagnetic Resonance (EPR) is used to detect the existence of $\cdot O_2^-$. As shown in Fig. 5d, BMPO, a classic capture agent was applied. In order to ensure the full oxidation of AgNWs and enough $\cdot O_2^-$ for detection, chronopotentiometry was used and the potential was set at 1.6 V. The EPR signal of conformer II of $\cdot O_2^-$ was detected in the electrolyte.[67] The generation of Ag–O can be verified by *in situ* Raman spectroscopy as demonstrated in Fig. 5e. As the potential increased to 0.6 V, peaks that appeared at 220 cm^{-1}, 300 cm^{-1}, 426 cm^{-1} and 467 cm^{-1} could be attributed to the stretching vibrations of Ag–O in AgO, while the peak at 486 cm^{-1} corresponds to the vibrations of Ag–O in the Ag_2O phase.[68] While increasing the potential to 0.9 V, the Raman signal was blocked due to the generation of bubbles. The test on the Au surface showed nearly the same peaks as those on the ITO surface, as shown in Fig. S15a. As presented in Fig. 5f, compared with AgNWs@Au at 0.7 V, a small peak at

around 930 cm^{-1} appeared on AgNWs@ITO, which can be associated with the vibration of O–O.[69] Fig. S15b shows that when *p*-BQ exists, no obvious Raman peak emerges, firmly confirming our conclusion.

Conclusions

In conclusion, we established a multimode imaging system that enables us to observe the interfacial electrochemical reaction concurrently from diverse perspectives. We designed an ITO-based Mott–Schottky junction, which incorporated ITO into the catalytic system and avoided analytical biases. *In situ* multimode observation showed that the high-valence oxidation of AgNWs occurred simultaneously with ECL, enabling the resolution of the reaction pathway mediated by superoxide radicals. The superoxide radical-consuming agents, such as luminol and *p*-BQ, exhibit a remarkable modulating effect on this unique reaction pathway. The EPR spectrum proves the very existence of superoxide radicals. Our research further revealed that the formation of Mott–Schottky junctions between AgNWs and ITO leads to charge transfer, enriching electrons on the surface of AgNWs. This charge accumulation effect, which is verified by the positive shift of PZC, influences the adsorption of substances at the AgNWs@ITO heterojunction interface, further affecting the high-valence oxidation of AgNWs, and finally alters the reaction pathway to a superoxide radical involved one. Our strategy provides an effective platform for *in situ* observation of Mott–Schottky junctions at the single nanoentity level and provides new ideas for reinforcing the fundamental comprehension of heterogeneous nano-catalytic reactions.

Author contributions

R. H. conceived and supervised the project. Y. C. performed the experiments and characterization. Y. C., L. W. and H. C. designed the experimental set-up. L. P. and Z. Z. assisted with substrate preparation and electrochemical data analysis, respectively. Y. C. wrote the manuscript.

Conflicts of interest

There are no conflicts to declare.

Data availability

The experimental procedures and supplementary data are provided in the supplementary information (SI). Supplementary information is available. See DOI: **https://doi.org/10.1039/d5sc06225j**.

Acknowledgements

We gratefully acknowledge financial support from the National Natural Science Foundation of China (22374064) and the Shenzhen Science and Technology Program (ZDSYS20230626090803004).

References

1 D. Xu, S.-N. Zhang, J.-S. Chen and X.-H. Li, Design of the Synergistic Rectifying Interfaces in Mott–Schottky Catalysts, *Chem. Rev.*, 2023, **123**, 1–30.
2 X. Xu, H. Liao, L. Huang, S. Chen, R. Wang, S. Wu, Y. Wu, Z. Sun and H. Huang, Surface reconstruction and directed electron transport in $NiSe_2/MoSe_2$ Mott-Schottky heterojunction catalysts promote urea-assisted water splitting, *Appl. Catal., B*, 2024, **341**, 123312.
3 Z. Sun, C. Li, J. Lin, T. Guo, S. Song, Y. Hu, Z. Zhang, W. Yan, Y. Wang, Z. Wei, F. Zhang, K. Zheng, D. Wang, Z. Li, S. Wang and W. Chen, Lattice Strain and Mott–Schottky Effect of the Charge-Asymmetry Pd1Fe Single-Atom Alloy Catalyst for Semi-Hydrogenation of Alkynes with High Efficiency, *ACS Nano*, 2024, **18**, 13286–13297.
4 H. Zhong, C. Yang, L. Fan, Z. Fu, X. Yang, X. Wang and R. Wang, Dyadic promotion of photocatalytic aerobic oxidation via the Mott–Schottky effect enabled by nitrogen-doped carbon from imidazolium-based ionic polymers, *Energy Environ. Sci.*, 2019, **12**, 418–426.
5 K.-X. Zhang, H. Su, H.-H. Wang, J.-J. Zhang, S.-Y. Zhao, W. Lei, X. Wei, X.-H. Li and J.-S. Chen, Atomic-Scale Mott–Schottky Heterojunctions of Boron Nitride Monolayer and Graphene as Metal-Free Photocatalysts for Artificial Photosynthesis, *Adv. Sci.*, 2018, **5**, 1800062.
6 Z. Huang, L. Chen, H. Zhang, M. Humayun, J. Duan, Q. Zhu, M. Bououdina, Y. Cao, Y. A. Attia, G. Kardas and C. Wang, Manipulating interfacial charge redistribution in Mott-Schottky electrocatalyst for high-performance water/seawater splitting, *Chem. Eng. J.*, 2024, **501**, 157628.
7 X.-H. Li and M. Antonietti, Metal nanoparticles at mesoporous N-doped carbons and carbon nitrides: functional Mott–Schottky heterojunctions for catalysis, *Chem. Soc. Rev.*, 2013, **42**, 6593–6604.
8 X. Lin, S.-N. Zhang, D. Xu, J.-J. Zhang, Y.-X. Lin, G.-Y. Zhai, H. Su, Z.-H. Xue, X. Liu, M. Antonietti, J.-S. Chen and X.-H. Li, Electrochemical activation of C–H by electron-deficient W_2C nanocrystals for simultaneous alkoxylation and hydrogen evolution, *Nat. Commun.*, 2021, **12**, 3882.
9 H. Li, Y. Lin, J. Duan, Q. Wen, Y. Liu and T. Zhai, Stability of electrocatalytic OER: from principle to application, *Chem. Soc. Rev.*, 2024, **53**, 10709–10740.
10 A. Grimaud, O. Diaz-Morales, B. Han, W. T. Hong, Y.-L. Lee, L. Giordano, K. A. Stoerzinger, M. T. M. Koper and Y. Shao-Horn, Activating lattice oxygen redox reactions in metal oxides to catalyse oxygen evolution, *Nat. Chem.*, 2017, **9**, 457–465.
11 Y. Song, W. Zhao, Z. Wang, W. Shi, F. Zhang, Z. Wei, X. Cui, Y. Zhu, T. Wang, L. Sun and B. Zhang, Sub-4 nm Ru-RuO_2 Schottky Nanojunction as a Catalyst for Durable Acidic Water Oxidation, *J. Am. Chem. Soc.*, 2025, **147**, 13775–13783.
12 Z. Zhang, X. Li, C. Zhong, N. Zhao, Y. Deng, X. Han and W. Hu, Spontaneous Synthesis of Silver-Nanoparticle-Decorated Transition-Metal Hydroxides for Enhanced

Oxygen Evolution Reaction, *Angew. Chem., Int. Ed.*, 2020, **59**, 7245–7250.

13 X. Lu, Z. Ma, Y. Chang, S. Wang, X. Li, D. Xu, J. Bao and Y. Liu, Mott–Schottky Construction Boosted Plasmon Thermal and Electronic Effects on the Ag/CoV-LDH Nanohybrids for Highly-Efficient Water Oxidation, *Adv. Mater.*, 2024, **36**, 2313057.

14 B. de la Fuente, D. A. Khurana, P. M. Vereecken, A. Hubin and T. Hauffman, Nano-TiO_2/TiN Systems for Electrocatalysis: Mapping the Changes in Energy Band Diagram across the Semiconductor|Current Collector Interface and the Study of Effects of TiO_2 Electrochemical Reduction Using UV Photoelectron Spectroscopy, *ACS Appl. Mater. Interfaces*, 2024, **16**, 49926–49934.

15 Y. Huang, X. Zhang, L. Li, M. Humayun, H. Zhang, X. Xu, S. P. Anthony, Z. Chen, J. Zeng, D. V. Shtansky, K. Huo, H. Song, C. Wang and W. Zhang, Mott–Schottky Barrier Enabling High-Performance Hydrazine-Assisted Hydrogen Generation at Ampere-Level Current Densities, *Adv. Funct. Mater.*, 2025, **35**, 2401011.

16 L. Li, G. Wang, M. Chen, T. Wang, H. Yang, J. Yu and Y. Zhang, Mott-Schottky junction mediated photothermal-pyroelectric synergy for effective collection of waste heat in flexible sensing platform, *Nano Energy*, 2024, **128**, 109911.

17 J. He, S. Chen, Z. Ma, M. Wang and Q. He, Spatial Identification of Mott–Schottky Effect at Electrocatalytic Pd/Metal Oxide Interfaces for the Oxygen Reduction Reaction, *ACS Nano*, 2024, **18**, 24283–24294.

18 C. Bie, Z. Meng, B. He, B. Cheng, G. Liu and B. Zhu, Exploring photogenerated charge carrier transfer in semiconductor/metal junctions using Kelvin probe force microscopy, *J. Mater. Sci. Technol.*, 2024, **173**, 11–19.

19 L. Lechaptois, Y. Prado and O. Pluchery, KPFM visualisation of the Schottky barrier at the interface between gold nanoparticles and silicon, *Nanoscale*, 2023, **15**, 7510–7516.

20 D. Rothhardt, C. Penschke, H. J. Hug, R. Hoffmann-Vogel and A. Kimouche, Edge-Energy-Driven Growth of Monolayer MnI_2 Islands on Ag(111): High-Resolution Imaging and Theoretical Analysis, *ACS Nano*, 2025, **19**, 2261–2267.

21 A. Biswas, S. Nandi, N. Kamboj, J. Pan, A. Bhowmik and R. S. Dey, Alteration of Electronic Band Structure via a Metal–Semiconductor Interfacial Effect Enables High Faradaic Efficiency for Electrochemical Nitrogen Fixation, *ACS Nano*, 2021, **15**, 20364–20376.

22 S. Wu, X. Tan, J. Lei, H. Chen, L. Wang and J. Zhang, Ga-Doped and Pt-Loaded Porous TiO_2–SiO_2 for Photocatalytic Nonoxidative Coupling of Methane, *J. Am. Chem. Soc.*, 2019, **141**, 6592–6600.

23 C. Wan, G. Li, J. Wang, L. Xu, D. g. Cheng, F. Chen, Y. Asakura, Y. Kang and Y. Yamauchi, Modulating Electronic Metal-Support Interactions to Boost Visible-Light-Driven Hydrolysis of Ammonia Borane: Nickel-Platinum Nanoparticles Supported on Phosphorus-Doped Titania, *Angew. Chem., Int. Ed.*, 2023, **62**, e202305371.

24 J.-F. Lemineur, H. Wang, W. Wang and F. Kanoufi, Emerging Optical Microscopy Techniques for Electrochemistry, *Ann. Rev. Anal. Chem.*, 2022, **15**, 57–82.

25 J. T. Mefford, A. R. Akbashev, M. Kang, C. L. Bentley, W. E. Gent, H. D. Deng, D. H. Alsem, Y.-S. Yu, N. J. Salmon, D. A. Shapiro, P. R. Unwin and W. C. Chueh, Correlative operando microscopy of oxygen evolution electrocatalysts, *Nature*, 2021, **593**, 67–73.

26 J. Ma, Z. Wang, B. Jiang, W. Wang and H. Wang, Directly Imaging and Regulating the Nanoscale Inhomogeneity of S-Vacancies in Molybdenum Disulfide Monolayer during Electrocatalytic Hydrogen Evolution, *Angew. Chem., Int. Ed.*, 2023, **62**, e202305846.

27 T. Chen, B. Dong, K. Chen, F. Zhao, X. Cheng, C. Ma, S. Lee, P. Zhang, S. H. Kang, J. W. Ha, W. Xu and N. Fang, Optical Super-Resolution Imaging of Surface Reactions, *Chem. Rev.*, 2017, **117**, 7510–7537.

28 D. Jiang, Y. Jiang, Z. Li, T. Liu, X. Wo, Y. Fang, N. Tao, W. Wang and H.-Y. Chen, Optical Imaging of Phase Transition and Li-Ion Diffusion Kinetics of Single $LiCoO_2$ Nanoparticles During Electrochemical Cycling, *J. Am. Chem. Soc.*, 2016, **139**, 186–192.

29 M. Zhao, W. Li, M. Yang, Z. Zhao, R. Ye, X. Mao, P. Padgett and P. Chen, Long-range enhancements of micropollutant adsorption on metal-promoted photocatalysts, *Nat. Catal.*, 2024, **7**, 912–920.

30 M. Suri, F. Salimi Jazi, J. C. Crowley, Y. Park, B. Fu, P. Chen, W. R. Zipfel, B. Barstow and T. Hanrath, Spatially resolved charge-transfer kinetics at the quantum dot–microbe interface using fluorescence lifetime imaging microscopy, *Proc. Natl. Acad. Sci. U. S. A.*, 2025, **122**, e2407987122.

31 S. Liu, H. Li, S. Fang, W. Xu, W. Hu and W. Wang, Spontaneous Takeoff of Single Sulfur Nanoparticles during Sublimation Studied by Dark-Field Microscopy, *J. Am. Chem. Soc.*, 2023, **145**, 3987–3993.

32 M. Suvira, A. Ahuja, P. Lovre, M. Singh, G. W. Draher and B. Zhang, Imaging Single H_2 Nanobubbles Using Off-Axis Dark-Field Microscopy, *Anal. Chem.*, 2023, **95**, 15893–15899.

33 B. Fuladpanjeh-Hojaghan, M. M. Elsutohy, V. Kabanov, B. Heyne, M. Trifkovic and E. P. L. Roberts, In-Operando Mapping of pH Distribution in Electrochemical Processes, *Angew. Chem., Int. Ed.*, 2019, **58**, 16815–16819.

34 J. Gao, R.-Y. Zhao, Y.-G. Wang, R.-C. Xie and W. Wang, Rapid fluorescent mapping of electrochemically induced local pH changes, *Adv. Sen. Energy Mater.*, 2022, **1**, 100030.

35 G. Zhang, X. Zou, Q. Wang and Y. He, Surface Curvature Dominated Guest-Induced Nonequilibrium Deformations of Single Covalent Organic Framework-300 Particles, *Angew. Chem., Int. Ed.*, 2022, **62**, e202214569.

36 Q. Wang, Y. Tao, Z. Li, W. Ye, Y. Wang, D. Liu and Y. He, Visualizing dynamic competitive adsorption processes between iodine and methyl iodide within single covalent organic framework crystals, *J. Hazard. Mater.*, 2024, **463**, 132841.

37 M. J. Lagos, A. Trügler, U. Hohenester and P. E. Batson, Mapping vibrational surface and bulk modes in a single nanocube, *Nature*, 2017, **543**, 529–532.

38 L. Tong, D. Li, T. Su, S. Gao, P. Wang, J. Tang, Z. L. Wang, K. Shi and Z. W. Wang, Direct mapping of bending and torsional dynamics in individual nanostructures, *Proc. Natl. Acad. Sci. U. S. A.*, 2023, **120**, e2221956120.

39 M. Saqib, Y. Fan, R. Hao and B. Zhang, Optical imaging of nanoscale electrochemical interfaces in energy applications, *Nano Energy*, 2021, **90**, 106539.

40 B. Jiang, H. Li, W. Wang and H. Wang, Optical in situ deciphering of the surface reconstruction–assistant multielectron transfer event of single Co_3O_4 nanoparticles, *Proc. Natl. Acad. Sci. U. S. A.*, 2024, **121**, e2407146121.

41 M. Moghaddam, L. Godeffroy, J. J. Jasielec, N. Kostopoulos, J. M. Noël, J. Y. Piquemal, J. F. Lemineur, P. Peljo and F. Kanoufi, Scanning Electrochemical Microscopy Meets Optical Microscopy: Probing the Local Paths of Charge Transfer Operando in Booster-Microparticles for Flow Batteries, *Small*, 2024, **20**, 2309607.

42 Y. Cui, X. Zhao, M. Saqib and R. Hao, Multimode imaging analysis of single particles at the electrochemical interfaces, *Curr. Opin. Electrochem.*, 2024, **46**, 101527.

43 X. Zhao, Y. Li, Y. Cui, M. Saqib, X. Zhang, R. Hao and Z. Zheng, Spatiotemporally and Chemically Resolved Imaging of Electrocatalytic Oxygen Evolution on Single Nanoplates of Cobalt-Layered Hydroxide, *J. Am. Chem. Soc.*, 2023, **145**, 20897–20906.

44 P. Ciocci, J.-F. Lemineur, J.-M. Noël, C. Combellas and F. Kanoufi, Differentiating electrochemically active regions of indium tin oxide electrodes for hydrogen evolution and reductive decomposition reactions. An in situ optical microscopy approach, *Electrochim. Acta*, 2021, **386**, 138498.

45 Z. Zhang, J. Dong, Y. Yang, Y. Zhou, Y. Chen, Y. Xu and J. Feng, Direct probing of single-molecule chemiluminescent reaction dynamics under catalytic conditions in solution, *Nat. Commun.*, 2023, **14**, 7993.

46 Y. Lyu, P. Mollik, A. L. Oláh and D. P. Halter, Construction and Evaluation of Cheap and Robust Miniature Ag/AgCl Reference Electrodes for Aqueous and Organic Electrolytes, *ChemElectroChem*, 2024, **11**, e202300792.

47 T. P. Dirkse, Standard Electrode Potential of the Ag_2O/Ag Electrodes in Alkaline Solutions at 25 °C, *J. Chem. Eng. Data*, 1961, **6**, 538–540.

48 R. Gao, M. A. Edwards, Y. Qiu, K. Barman and H. S. White, Visualization of Hydrogen Evolution at Individual Platinum Nanoparticles at a Buried Interface, *J. Am. Chem. Soc.*, 2020, **142**, 8890–8896.

49 L. S. D. Antony, L. Monin, M. Aarts and E. Alarcon-Llado, Unveiling Nanoscale Heterogeneities at the Bias-Dependent Gold–Electrolyte Interface, *J. Am. Chem. Soc.*, 2024, **146**, 12933–12940.

50 M. Xi, Z. Wu, Z. Luo, L. Ling, W. Xu, R. Xiao, H. Wang, Q. Fang, L. Hu, W. Gu and C. Zhu, Water Activation for Boosting Electrochemiluminescence, *Angew. Chem., Int. Ed.*, 2023, **62**, e202302166.

51 Y. Wei, X. Fan, D. Chen, X. Zhu, L. Yao, X. Zhao, X. Tang, J. Wang, Y. Zhang, T. Qiu and Q. Hao, Probing Oxidation Mechanisms in Plasmonic Catalysis: Unraveling the Role of Reactive Oxygen Species, *Nano Lett.*, 2024, **24**, 2110–2117.

52 Q. Shen, J. Chen, X. Jing and C. Duan, Polyoxometalate-Embedded Metal–Organic Framework as an Efficient Copper-Based Monooxygenase for $C(sp^3)$–H Bond Oxidation via Multiphoton Excitation, *ACS Catal.*, 2023, **13**, 9969–9978.

53 S.-C. Huang, X. Wang, Q.-Q. Zhao, J.-F. Zhu, C.-W. Li, Y.-H. He, S. Hu, M. M. Sartin, S. Yan and B. Ren, Probing nanoscale spatial distribution of plasmonically excited hot carriers, *Nat. Commun.*, 2020, **11**, 4211.

54 H. Li, X. Zhang, Z. Sun and W. Ma, Rapid Screening of Bimetallic Electrocatalysts Using Single Nanoparticle Collision Electrochemistry, *J. Am. Chem. Soc.*, 2022, **144**, 16480–16489.

55 I. R. Zamora-Garcia, A. Alatorre-Ordaz, J. G. Ibanez, M. G. Garcia-Jimenez, Y. Nosaka, T. Kobayashi and S. Sugita, Thermodynamic and electrochemical study on the mechanism of formation of $Ag(OH)_4^-$ in alkaline media, *Electrochim. Acta*, 2013, **111**, 268–274.

56 X. Che, S. Wang, C. Li, G. Wang, C. Li, S. Wang, D. Li and J. Qiu, Inverted Capacitive Deionization with Highly Enhanced Stability Performance Utilizing Ionic Liquid-Functionalized Carbon Electrodes, *ACS Sustain. Chem. Eng.*, 2019, **7**, 15715–15722.

57 K. A. Soliman and L. A. Kibler, Variation of the potential of zero charge for a silver monolayer deposited onto various noble metal single crystal surfaces, *Electrochim. Acta*, 2007, **52**, 5654–5658.

58 K. A. Soliman, L. A. Kibler and D. M. Kolb, Electrocatalytic Behaviour of Epitaxial Ag(111) Overlayers Electrodeposited onto Noble Metals: Electrooxidation of d-Glucose, *Electrocatalysis*, 2012, **3**, 170–175.

59 O. A. Petrii, Zero charge potentials of platinum metals and electron work functions (Review), *Russ. J. Electrochem.*, 2013, **49**, 401–422.

60 O. Sufiani, J. Elisadiki, H. Tanaka, K. Teshima, M. G. Sahini, R. L. Machunda and Y. A. C. Jande, Adsorption-capacitive deionization hybrid system with activated carbon of modified potential of zero charge, *Environ. Res.*, 2023, **219**, 115114.

61 M. Kim, E. Batsa Tetteh, O. A. Krysiak, A. Savan, B. Xiao, T. H. Piotrowiak, C. Andronescu, A. Ludwig, T. Dong Chung and W. Schuhmann, Acidic Hydrogen Evolution Electrocatalysis at High-Entropy Alloys Correlates with its Composition-Dependent Potential of Zero Charge, *Angew. Chem., Int. Ed.*, 2023, **62**, e202310069.

62 H. Tüysüz, Alkaline Water Electrolysis for Green Hydrogen Production, *Acc. Chem. Res.*, 2024, **57**, 558–567.

63 Z. Y. Yu, Y. Duan, X. Y. Feng, X. Yu, M. R. Gao and S. H. Yu, Clean and Affordable Hydrogen Fuel from Alkaline Water Splitting: Past, Recent Progress, and Future Prospects, *Adv. Mater.*, 2021, **33**, 2007100.

64 W. Liu, Y. Li, F. Liu, W. Jiang, D. Zhang and J. Liang, Visible-light-driven photocatalytic degradation of diclofenac by carbon quantum dots modified porous g-C_3N_4: Mechanisms, degradation pathway and DFT calculation, *Water Res.*, 2019, **151**, 8–19.

65 W.-D. Oh, L.-W. Lok, A. Veksha, A. Giannis and T.-T. Lim, Enhanced photocatalytic degradation of bisphenol A with Ag-decorated S-doped g-C_3N_4 under solar irradiation: Performance and mechanistic studies, *Chem. Eng. J.*, 2018, **333**, 739–749.

66 Y. Fu, T. Huang, L. Zhang, J. Zhu and X. Wang, Ag/g-C_3N_4catalyst with superior catalytic performance for the degradation of dyes: a borohydride-generated superoxide radical approach, *Nanoscale*, 2015, **7**, 13723–13733.

67 J. Chang, R. D. Taylor, R. A. Davidson, A. Sharmah and T. Guo, Electron Paramagnetic Resonance Spectroscopy Investigation of Radical Production by Gold Nanoparticles in Aqueous Solutions Under X-ray Irradiation, *J. Phys. Chem. A*, 2016, **120**, 2815–2823.

68 J. Liu, X. Sang, P. Zhao, J. Li, S. Li, H. Dong, X. Zhou, M. Liu and W. You, Constructing AgO/Ag_2O Electrocatalysts with Highly Exposed and Tightly Contacted Active Facets for Efficient Oxygen Evolution, *Chem. – Eur. J.*, 2025, **31**, e202402951.

69 C.-B. Wang, G. Deo and I. E. Wachs, Interaction of Polycrystalline Silver with Oxygen, Water, Carbon Dioxide, Ethylene, and Methanol: In Situ Raman and Catalytic Studies, *J. Phys. Chem. B*, 1999, **103**, 5645–5656.